

## References and Notes

1. F. Liebau, *Structural Chemistry of Silicates* (Springer-Verlag, Berlin, 1985).
2. J. F. Stebbins and P. F. McMillan, *J. Non-Cryst. Solids* **160**, 116 (1993); *Am. Mineral.* **74**, 965 (1989).
3. R. M. Laine *et al.*, *Nature* **353**, 642 (1991); *J. Mater. Chem.* **6**, 1441 (1996).
4. K. Y. Blohowiak *et al.*, *Chem. Mater.* **6**, 2177 (1994).
5. M. L. Hoppe, R. M. Laine, J. Kampf, M. S. Gordon, L. W. Burggraf, *Angew. Chem. Int. Ed. Engl.* **32**, 287 (1993).
6. B. Herreros, S. W. Carr, J. Klinowski, *Science* **263**, 1585 (1994).
7. C. Chuit, R. J. P. Corriu, C. Reyé, J. C. Young, *Chem. Rev.* **93**, 1371 (1993).
8. G. J. Gainsford, T. Kemmitt, N. B. Milestone, *Acta Crystallogr. C* **51**, 8 (1995); T. Kemmitt and N. B. Milestone, *Aust. J. Chem.* **48**, 93 (1995).
9. J. H. Small, K. J. Shea, D. A. Loy, G. M. Jamison, *ACS Symp. Ser.* **585**, 248 (1995).
10. A. Rosenheim, B. Reibmann, G. Schendel, *Z. Anorg. Chem.* **196**, 160 (1931); I. F. Sedeh, S. Sjöberg, L. O. Öhman, *Acta Chem. Scand.* **46**, 933 (1992); *J. Inorg. Biochem.* **50**, 119 (1993).
11. A. Weiss and D. R. Harvey, *Angew. Chem.* **76**, 818 (1964).
12. S. Sjöberg, N. Ingri, A. M. Nenner, L. O. Öhman, *J. Inorg. Biochem.* **24**, 267 (1985); D. F. Evans, J. Parr, C. Y. Wong, *Polyhedron* **11**, 567 (1992).
13. S. D. Kinrade, K. J. Maa, A. S. Schach, T. A. Sloan, C. T. G. Knight, *J. Chem. Soc. Dalton Trans.*, in press; S. D. Kinrade, C. T. G. Knight, D. L. Pole, R. T. Svytski, *Inorg. Chem.* **37**, 4272 (1998); *ibid.*, p. 4278; C. T. G. Knight, *Zeolites* **9**, 448 (1989).
14. It has become accepted in the literature that four-coordinate silicate centers are denoted by a "Q" for quadrifunctional. The extent of protonation is ignored, and a superscript is used to indicate the number of shared siloxane linkages. Choosing symbols for the five- and six-coordinate centers that are, at once, systematic and practical to use is difficult. The Latin prefix quinti- presents an obvious problem. Herreros *et al.* (6) used a Roman superscript to indicate five-coordinate sites, for example Si<sup>v</sup>, but such a system becomes unwieldy describing other than symmetric silicate species. We propose using Greek prefixes to describe the state of Si coordination, obtaining "P" for pentafunctional and "H" for hexafunctional. This terminology is immediately understandable and avoids use of unusual typographical symbols. Over- or underscoring the labels is recommended to avoid confusion with the corresponding elements. Thus, the monomeric species represented by the resonances in Fig. 1 would be labeled as Q<sup>o</sup>, P<sup>o</sup>, and H<sup>o</sup>.
15. That is, only when there are two adjacent hydroxy groups occurring on opposite sides of the molecule's Fischer projection (Fig. 3).
16. For low-alkalinity solutions ([OH<sup>-</sup>]:[SiO<sub>2</sub>] ≤ 1:1), the <sup>13</sup>C NMR signals corresponding to Si-coordination sites on the polyol shift up-frequency by 1 to 3 ppm from their bulk solution values. Thus, whereas free D-threitol resonates at 62.9 (C-1,4) and 71.8 ppm (C-2,3), the major threitol-Si complex resonates at 64.7, 64.9 (-OSi coordinated C-1,4), 70.7, and 71.7 ppm (C-2,3). Similarly, only the C-2,5 signals of D-mannitol move up-frequency upon silicate complexation, shifting from 71.4 ppm to 74.2 and 74.5 ppm.
17. Carbon-13 NMR investigations into the interaction between aqueous borates and polyols reveal similar high-frequency shifts upon complex formation [A. Munoz and L. Lamandé, *Carbohydrate Res.* **225**, 113 (1991)]. Consistent with our observations, the structural criterion for optimal borate complex formation appears to be that the polyols contain a *threo* hydroxy pair. However, the boron center appears to bind across the *threo* pair itself, rather than at sites adjacent to it. Moreover, boron does not undergo an increase in coordination number.
18. As the [OH<sup>-</sup>]:[SiO<sub>2</sub>] ratio of solutions containing D-threitol is raised above 1:1, new <sup>13</sup>C NMR signals occur at 66.0 (C-1,4) and 70.2 ppm (C-2,3).
19. S. D. Kinrade, *J. Phys. Chem.* **100**, 4760 (1996); I. L. Svensson, S. Sjöberg, L.-O. Öhman, *J. Chem. Soc. Faraday Trans.* **31**, 4558 (1989).
20. J. J. R. Frausto da Silva and R. P. J. Williams, *The*

*Biological Chemistry of the Elements* (Clarendon, Oxford, 1991); R. K. Iler, *The Chemistry of Silica* (Wiley, New York, 1979).

21. J. D. Birchall, *Chem. Soc. Rev.* **24**, 351 (1995).
22. We thank J. T. Banks for helpful discussions and R. J. Kirkpatrick for the generous loan of isotopically enriched silica. Funding was provided in part by NIH

(PHS 1 S10 RR 10444-01; GM-42208 and RR 01811), NSF (NSF CHE 96-10502), and the Natural Sciences and Engineering Council of Canada (NSERC). Facilities were provided by the NIH-supported Illinois EPR Research Center, and the NSERC-supported Prairie Regional NMR Centre (Winnipeg).

23 February 1999; accepted 15 July 1999

## Seismic Velocity and Density Jumps Across the 410- and 660-Kilometer Discontinuities

Peter M. Shearer<sup>1\*</sup> and Megan P. Flanagan<sup>2</sup>

The average seismic velocity and density jumps across the 410- and 660-kilometer discontinuities in the upper mantle were determined by modeling the observed range dependence in long-period seismic wave arrivals that reflect off of these interfaces. The preliminary reference Earth model (PREM) is within the computed 95 percent confidence ellipse for the 410-km discontinuity but outside the allowed jumps across the 660-kilometer discontinuity. Current pyrolite mantle models appear consistent with the constraints for the 410-kilometer discontinuity but overpredict amplitudes for the 660-kilometer reflections. The density jump across the 660-kilometer discontinuity is between 4 and 6 percent, below the PREM value of 9.3 percent commonly used in mantle convection calculations.

Observed seismic velocity discontinuities near 410- and 660-km depth in Earth's upper mantle are believed to be caused primarily by phase changes in olivine and other minerals that result from the increasing pressure with increasing depth (1). Resolving the details of the discontinuities is important for modeling the composition of the mantle and for understanding the effect that the discontinuities may have on mantle convection (2). Recent analyses of reflected seismic phases (3–5) have yielded estimates of the average discontinuity depths that agree within ±1%; in contrast, the average P and S velocity increases across the boundaries are known less precisely, and differences of a factor of 2 or greater are seen in the velocity jumps obtained in different studies (6). The density jumps, critical parameters for modeling of mantle dynamics, are particularly hard to measure and are often based on velocity versus density scaling relations rather than direct observational measurements.

In principle, however, the velocity and density jumps can be separately resolved by studying the behavior of reflection coefficients (7) as a function of ray angle. Following this approach, we used the observed amplitudes of reflections off the bottom of the 410- and 660-

km discontinuities to measure the velocity and density jumps across the interfaces. These reflections occur as precursors to the phases SS and PP in long-period seismograms (8). Our data consisted of 13,469 transverse-component and 24,667 vertical-component seismograms from the global seismic networks (GDSN, IRIS, and Geoscope) recorded between 1976 and 1997. To enhance the visibility of the discontinuity reflections, we aligned the seismograms on the maximum amplitude of SS (for the transverse components) and PP (for the vertical components) and stacked the data in bins of constant source-receiver range (Fig. 1). The underside reflected phases S410S and S660S were visible in the transverse-component stack, arriving 2 to 4 min before the direct SS phase. The underside P reflection off the 410-km discontinuity, P410P, was observed in the vertical-component stack between 100° and 145°, but the underside 660-km reflection, P660P, was not seen (9, 10). Additional details concerning the data and our stacking methods may be found in previous studies (4, 11, 12).

We measured the relative amplitudes between the discontinuity reflections and the reference phases SS and PP within 1° bins in source-receiver distance across the intervals for which arrivals were visible (112° to 160° for S410S, 118° to 165° for S660S, and 102° to 140° for P410P). Because of interference from PKP, we did not use P410P data between 118° and 130°. Although P660P was not visible, limits could still be placed on its average amplitude between 118° and 122°, where interference from other phases is ab-

<sup>1</sup>Institute of Geophysics and Planetary Physics, Scripps Institution of Oceanography, University of California, San Diego, La Jolla, CA 92093–0225, USA.

<sup>2</sup>Lawrence Livermore National Laboratory, Post Office Box 808, L-206, Livermore, CA 94551, USA.

\*To whom correspondence should be addressed.

## REPORTS

sent. The amplitudes of discontinuity reflections in these stacks were reduced somewhat by incoherent stacking resulting from small time shifts in the reflected phases (3, 9). We adjusted for this effect by increasing the measured amplitudes by 14% to more closely approximate the true reflection amplitudes (13). Finally, it should be noted that the “discontinuities” may actually involve enhanced velocity and density gradients over finite depth intervals rather than sharp interfaces (14). Because our observations are at long periods, however, this effect reduces the amplitudes of the reflected pulses by less than 7% for depth intervals up to 20 km and reduces the amplitudes by less than 13% for

depth intervals up to 30 km (15).

We estimated the error bounds for the measured amplitudes using a bootstrap resampling method (16) where we repeated the stack of the traces 200 times using random subsets of the data. The  $S410S/SS$  and  $S660S/SS$  amplitude ratios vary from about 0.02 to 0.05, with a slight increase in amplitude with range (Fig. 2).  $P410P/PP$  amplitudes show more scatter but appear approximately constant with range. The  $P660P/PP$  amplitudes near  $120^\circ$  are small ( $<0.008$ ), and zero  $P660P$  amplitudes are included within our error bounds.

To model our observations, we computed synthetic seismograms based on the prelimi-

nary reference Earth model (PREM) (17). We used a theoretical ray method that includes geometrical spreading and attenuation. Because of the ray path similarity between the precursors and the main phases, the reflection coefficient at the discontinuities was the main factor controlling the theoretical  $SdS/SS$  and  $PdP/PP$  amplitudes (8). For the 410-km discontinuity, the PREM predictions fit most of the observations within their error bounds (Fig. 2, A and B), although the slope of the amplitude increase with range seen in the  $S410S/SS$  observations is underpredicted. For the 660-km discontinuity, however, the PREM predictions lie outside the observed error bounds (Fig. 2, C and D). PREM predicts a clear  $P660P$  phase near  $120^\circ$ , whereas no such phase is seen in the data (10). A mismatch is also seen in the  $S660S$  amplitudes, where PREM predicts amplitude ratios almost twice those that are observed.

Because the amplitudes of the  $SS$  and  $PP$  precursors are mainly determined by the reflection coefficients at the discontinuities, their amplitudes may be approximated by varying three parameters: the  $P$  velocity jump ( $\Delta\alpha$ ), the  $S$  velocity jump ( $\Delta\beta$ ), and the density jump ( $\Delta\rho$ ) at the discontinuities. We explored this parameter space by computing synthetic amplitudes for every combination of  $\Delta\alpha$ ,  $\Delta\beta$ , and  $\Delta\rho$  at 0.1% intervals between 0 and 10% [here we take  $\Delta\alpha$  and so forth to indicate the fractional change, for example,  $\Delta\alpha = 2(\alpha_2 - \alpha_1)/(\alpha_1 + \alpha_2)$ ]. We used PREM as a starting model for the mean values of  $\alpha$ ,  $\beta$ , and  $\rho$  across the boundaries and to compute the ray paths to and from the discontinuity reflection points.

For each combination of  $\Delta\alpha$ ,  $\Delta\beta$  and  $\Delta\rho$ , we compared our synthetic predictions with the observations for the  $SdS$  and  $PdP$  amplitudes and applied  $\chi^2$  statistics to our estimated errors to define  $1\sigma$  and  $2\sigma$  confidence ellipsoids. In performing this fit, our estimated errors for the observed  $SdS$  amplitudes needed to be scaled upward by 20% to yield an appropriate value of  $\chi^2$  at the best fitting point (suggesting that our original error estimates were too small); the estimated  $PdP$  errors required no adjustment. In addition to the formal error bounds (Fig. 3), some uncertainty is also associated with the correction for incoherent stacking. This uncertainty is difficult to quantify precisely, but we estimate that it is unlikely to alter the amplitudes shown in Figs. 2 and 3 by more than about 20% (18).

Only a small fraction of the models considered lie within the  $2\sigma$  (95% confidence) limits, but the confidence ellipsoids are elongated, indicating strong trade-offs between the model parameters. The allowed  $S$  and  $P$  velocity jumps across the 410-km discontinuity are correlated ( $\Delta\beta \approx 1.3\Delta\alpha$ ), and the density jump is inversely correlated with the

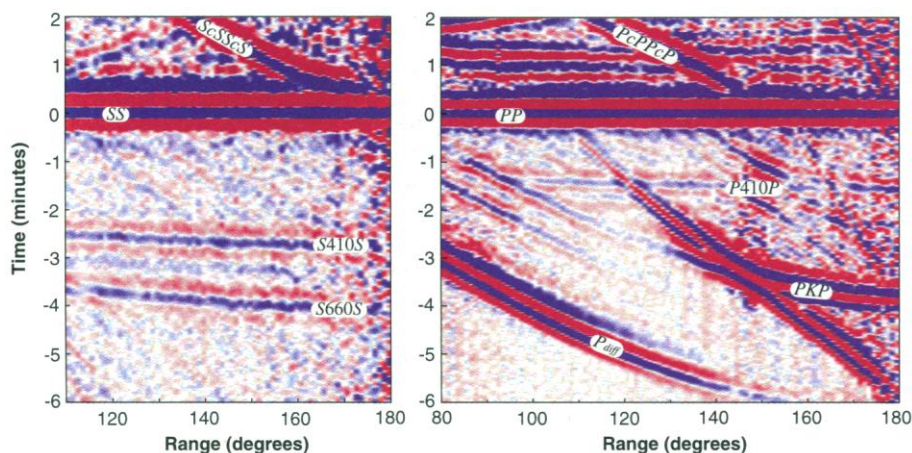


**Fig. 1.** Stacks of  $SS$  (left) and  $PP$  (right) precursors derived from over 30,000 long-period seismograms. The  $SS$  and  $PP$  reference phases are aligned at zero time. Amplitudes are shown relative to the reference phase, with positive amplitudes in blue and negative amplitudes in red. The precursors are underside reflections off the 410- and 660-km discontinuities that arrive several minutes before the main phase.

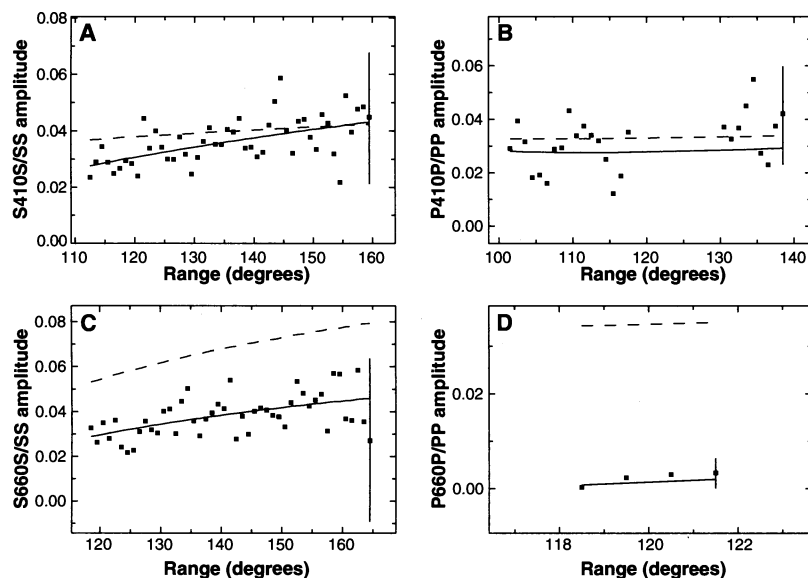


**Fig. 2.** Observed  $SS$  and  $PP$  precursor amplitudes are shown as squares with  $2\sigma$  error bars for (A)  $S410S/SS$ , (B)  $P410P/PP$ , (C)  $S660S/SS$ , and (D)  $P660P/PP$  amplitudes. For comparison, the solid lines show amplitudes predicted by PREM; the dashed lines show predicted amplitudes for our best fitting model. PREM fits the 410-km discontinuity data reasonably well but does not fit the observations for the 660-km discontinuity.

## REPORTS

$P$  and  $S$  velocity jumps (for example,  $\Delta\rho \approx 6.3\% - 0.7\Delta\alpha$ ). The PREM values for the 410-km discontinuity ( $\Delta\alpha = 2.5\%$ ,  $\Delta\beta = 3.4\%$ ,  $\Delta\rho = 5.0\%$ ) lie near the  $2\sigma$  confidence limit but would require only minor adjustments to fit within the  $1\sigma$  limits. Better fits to the data can be obtained with somewhat larger  $P$  and  $S$  velocity jumps and smaller density jumps than the PREM model; in fact, PREM has unusually small velocity jumps at 410-km compared with most models (6). Our best fitting model for the 410-km discontinuity ( $\Delta\alpha = 7.3\%$ ,  $\Delta\beta = 9.7\%$ ,  $\Delta\rho = 0.9\%$ ) has higher velocity jumps and a smaller density jump than most current models (6) but should not be preferred over other models within the  $1\sigma$  limits. Our  $2\sigma$  limits for the 410-km discontinuity include shear impedance contrasts (19) ranging from 6 to 12%, roughly consistent with earlier studies of  $ScS$  reverberations (3) and  $SS$  precursors (11), which suggested shear impedance changes at 410 km of  $9.2 \pm 2\%$  and  $6.7 \pm 1.1\%$ , respectively.

For the 660-km discontinuity, our computed confidence ellipsoids are also elongated. In this case, however, the PREM model ( $\Delta\alpha = 4.6\%$ ,  $\Delta\beta = 6.5\%$ ,  $\Delta\rho = 9.3\%$ ) lies outside the  $2\sigma$  limits, as might be anticipated from the poor fit to our observations that PREM predicts (Fig. 2). The absence of  $P660P$  in long-period stacks, particularly near  $120^\circ$ , where the images are free of other seismic phases, was shown by Estabrook and Kind (10) to imply a small velocity jump across the 660-km discontinuity. To explain the absence of  $P660P$ , Estabrook and Kind (10) proposed the EK1 model ( $\Delta\alpha = 2.5\%$ ,  $\Delta\beta = 6.1\%$ ,  $\Delta\rho = 6.2\%$ ), which has considerably smaller velocity and density jumps than PREM. The EK1 model lies outside our  $2\sigma$  confidence limits but is much closer to them than PREM. Our best-fitting model for the 660-km discontinuity has  $\Delta\alpha = 2.0\%$ ,  $\Delta\beta = 4.8\%$ , and  $\Delta\rho = 5.2\%$ ; however, the  $1\sigma$  limits include models with a range of other values. Our results support the hypothesis of Estabrook and Kind (10) that the change in bulk modulus across the 660-km discontinuity is small; the trade-off between  $\Delta\alpha$  and  $\Delta\beta$  (Fig. 3) is close to that predicted for zero change in bulk modulus. Because of the steep angle of the error ellipsoid to the density axis, limits on the density jump at 660 km are tighter than the corresponding velocity limits, and  $\Delta\rho$  is constrained to lie between 4.1 and 6.2% with 95% confidence. The preferred density jump of about 5% is substantially less than the PREM value of 9.3%. Our  $2\sigma$  limits for the 660-km discontinuity include shear impedance contrasts ranging from 7 to 13%, roughly consistent with earlier studies of  $ScS$  reverberations (3) and  $SS$  precursors (11), which suggested shear impedance changes at 660 km of  $14.4 \pm 2\%$  and  $9.9 \pm 1.5\%$ , respectively.

Our modeling results assume a simple first-order change in velocity and density across the 410- and 660-km discontinuities. The long-period reflections, however, cannot distinguish between a sharp interface and a more gradual change within layers up to about 20 km thick (15). In this case, the velocity and density changes cited here represent the total change over this depth interval. If multiple discontinuities are present, then our results could be biased by interference effects, particularly if the discontinuities are at depth intervals between about 30 and 80 km, where they could destructively interfere without being resolvable as separate pulses.

Bulk properties of different minerals determined from experiments at high temperature and pressure, including the phase changes known to occur near 410- and 660-km depth, are often compared with seismic velocity and density profiles to infer the composition and temperature of the mantle (20–22). The density and  $S$  velocity jumps at 410 km predicted by a pyrolite model containing 55% by volume olivine were recently shown (23) to agree with seismic observations of the shear impedance change at 410 km, whereas a more garnet-rich piclogite model (20) containing 35% olivine was only marginally consistent with the data. Our analysis supports this result; the pyrolite model fits the density and  $S$  velocity constraints at 410 km better than the piclogite model (Fig. 3A). The velocity and density jumps at 410 km in these models are controlled primarily by the fraction of olivine in the mantle (23); our observations would be best fit with a pyrolite

mantle containing  $\sim 50\%$  olivine. Our observations for the 660-km discontinuity are more difficult to reconcile with mineral physics results. The density and  $P$  velocity jumps at 660 km recently predicted for a pyrolite mantle (24) are substantially larger than our observed constraints (Fig. 3B) (25). Our observed absence of a large change in bulk modulus across the 660-km discontinuity appears consistent with some piclogite models (10, 21); however, more complete forward modeling will be required to test whether specific compositional models exist that can satisfy all of our seismic constraints.

The total density increase through the transition zone (410 to 660 km) must be sufficient to fit the constraints provided by Earth's total mass, moment of inertia, and normal-mode observations; a shortfall in density increase across 660 km compared with PREM must be accommodated by increased density gradients elsewhere in the transition zone. It is possible that at least some of the required density increase could occur at the 520-km discontinuity [absent in PREM but indicated by several recent studies (3–5, 11, 26)], where a density increase of 2 to 3% seems likely (11, 27). Finally, the density jump across 660 km is an important factor in mantle convection calculations (2) that include the effect of a phase boundary at 660 km. Because this phase boundary is believed to have a negative Clapeyron slope, the 660-km discontinuity acts to resist thermally driven flow across the interface, as buoyancy forces result from deflection of the phase boundary. In several numerical simulations (which assume near PREM values for the

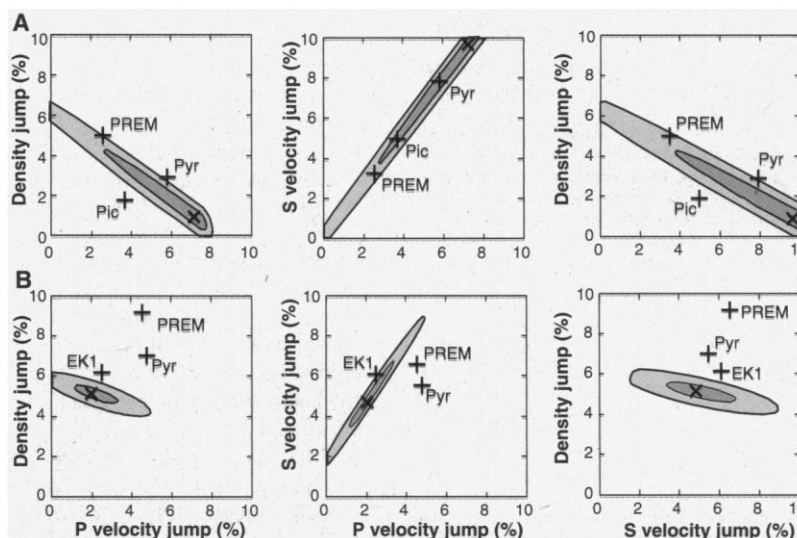


**Fig. 3.** Projections of the confidence ellipsoids for fits to the observations resulting from variations in  $P$  velocity,  $S$  velocity, and density across the (A) 410- and (B) 660-km discontinuities. The  $1\sigma$  and  $2\sigma$  limits are shown as dark and light gray, respectively. Our best fitting model is shown as a  $\times$  symbol. The PREM and EK1 models (10, 17) are indicated with pluses. The points labeled "Pyr" and "Pic" in (A) are the pyrolite and piclogite models, respectively, of Gaherty *et al.* (23), where the 410-km phase transition occurs over a 10-km interval. The points labeled "Pyr" in (B) are the pyrolite model of Weidner and Wang (24), computed for 5% Al and 1700 K.

660-km density jump), these forces are strong enough to produce partial layering in the mantle. The strength of the buoyancy forces, however, is proportional to the assumed density contrast across the interface. If the density contrast across the 660-km discontinuity is only 5%, as our results suggest, then layered convection is less likely.

References and Notes

1. Many authors, including A. E. Ringwood, *Composition and Petrology of the Earth's Mantle* (McGraw-Hill, New York, 1975); L.-G. Liu, *Nature* **262**, 770 (1976); I. Jackson, *Earth Planet. Sci. Lett.* **62**, 91 (1983); T. Katsura and E. Ito, *J. Geophys. Res.* **94**, 15663 (1989); E. Ito, M. Akaogi, L. Topor, A. Navrotsky, *Science* **249**, 1275 (1990).
2. U. R. Christensen and D. A. Yuen, *J. Geophys. Res.* **90**, 10291 (1985); P. Machetel and P. Weber, *Nature* **350**, 55 (1991); P. J. Tackley, D. J. Stevenson, G. A. Glatzmaier, G. Schubert, *ibid.* **361**, 699 (1993); S. Honda, D. A. Yuen, S. Balachandrar, D. Reuteler, *Science* **259**, 1308 (1993); L. P. Solheim and W. R. Peltier, *J. Geophys. Res.* **99**, 15861 (1994); P. J. Tackley, D. J. Stevenson, G. A. Glatzmaier, G. Schubert, *ibid.*, p. 15877; J. Ita and S. D. King, *ibid.*, p. 15919; C. Thoraval, P. Machetel, A. Cazenave, *Nature* **375**, 777 (1995).
3. J. S. Revenaugh and T. J. Jordan, *J. Geophys. Res.* **96**, 19763 (1991).
4. M. P. Flanagan and P. M. Shearer, *ibid.* **103**, 2673 (1998).
5. Y. Gu, A. M. Dziewonski, C. B. Agee, *Earth Planet. Sci. Lett.* **157**, 57 (1998).
6. G. Nolet and M. J. R. Wortel, in *The Encyclopedia of Solid Earth Geophysics*, D. E. James, Ed. (Van Nostrand Reinhold, New York, 1989), pp. 775-788; G. Nolet, S. P. Grand, B. L. N. Kennett, *J. Geophys. Res.* **99**, 23753 (1994).
7. The reflection coefficient is the ratio of the reflected wave amplitude to the incident wave amplitude.
8. *SS* and *PP* are the multiples of the direct *S* and *P* phases that contain a single reflection off Earth's surface midway between source and receiver. The precursors to *SS* and *PP* resulting from underside reflections off a discontinuity at depth *d* are termed *SdS* and *PdP*, respectively. For example, *S410S* indicates the *S* reflection off the bottom of the 410-km discontinuity.
9. P. M. Shearer, *J. Geophys. Res.* **96**, 18147 (1991).
10. C. H. Estabrook and R. Kind, *Science* **274**, 1179 (1996).
11. P. M. Shearer, *J. Geophys. Res.* **101**, 3053 (1996).
12. M. P. Flanagan and P. M. Shearer, *Geophys. Res. Lett.* **26**, 549 (1999).
13. We obtained this factor by computing the effect of time shifts on the amplitude of the *SS* and *PP* reference pulses in the stacks, assuming that the time shifts have a Gaussian distribution characterized by a standard deviation,  $\sigma$ . The time shifts result from differences in the two-way surface-to-discontinuity travel times caused by both discontinuity topography and upper mantle velocity heterogeneity. In general,  $\sigma$  will vary depending on the wave type (for example, *P* or *S*) and the geographic diversity of ray geometries in the stack. For *ScS* waves,  $\sigma = 4$  s was obtained for mixed continental and oceanic paths (3), whereas  $\sigma = 2.5$  s has been estimated for *SdS* waves in purely oceanic regions (17). The limited distribution of reflection points contained within each of our source-receiver range bins is likely to decrease  $\sigma$ , whereas the mixture of continental and oceanic points is likely to increase  $\sigma$ . For  $\sigma$  values of 2, 3, and 4 s, *SdS* amplitudes in our stacks are reduced by 8, 16, and 28%, respectively. The time shifts for *PdP* phases are likely to be smaller than those for *SdS*. For  $\sigma$  values of 1.0, 1.7, and 2.5 s, *PdP* amplitudes are reduced by 4, 12, and 23%, respectively. Our amplitude corrections are based on  $\sigma = 2.5$  s for *SdS* and  $\sigma = 1.7$  s for *PdP*.
14. G. Helffrich and B. J. Wood, *Geophys. J. Int.* **126**, F7 (1996); L. Stixrude, *J. Geophys. Res.* **102**, 14835 (1997).
15. For linear velocity and density gradients, our ob-

- served *SdS* and *PdP* amplitudes are reduced by 1 to 2% for a 10-km interval (compared with a sharp discontinuity), 3 to 7% for a 20-km interval, 6 to 13% for a 30-km interval, and 11 to 22% for a 40-km interval. The effect is largest where the velocities near the discontinuity are the smallest (that is, for *S410S*) and smallest where the velocities are the largest (that is, for *P660P*), although the *S* versus *P* difference is lessened in our case by the higher frequency content in the *PP* stack (the *SS* data have a dominant period of 30 s; the *PP* data are peaked at a 21-s period). Nonlinear gradients, which may occur for mantle phase transitions (14), will produce smaller amplitude reductions for reflected pulses than linear gradients over the same depth interval. Thus, these numbers represent upper bounds; the actual amplitude reductions may be smaller.
16. B. Efron and R. Tibshirani, *Science* **253**, 390 (1991).
17. A. M. Dziewonski and D. L. Anderson, *Phys. Earth Planet. Inter.* **25**, 297 (1981).
18. Values of the incoherent stacking parameter ranging from  $\sigma = 0$  s (perfect coherence) to 1.6 times larger than our preferred values (for example,  $\sigma = 4$  s for *SdS* waves and  $\sigma = 2.7$  s for *PdP* waves) resulted in adjusted amplitudes that varied by less than 20% from our computed amplitudes.
19. The shear impedance is the product of the shear velocity and density; thus, the shear impedance contrast is given by the sum of the *S* velocity and density jumps.
20. T. S. Duffy and D. L. Anderson, *J. Geophys. Res.* **94**, 1895 (1989).
21. J. Ita and L. Stixrude, *ibid.* **97**, 6849 (1992).

22. H. Fujisawa, *ibid.* **103**, 9591 (1998).
23. J. B. Gaherty, Y. Wang, T. H. Jordan, D. J. Weidner, *Geophys. Res. Lett.* **26**, 1641 (1999). This paper contains the changes in density and *S* velocity at 410 km for pyrolyte and piclogite models. Corresponding values for the changes in *P* velocity were obtained from J. B. Gaherty (personal communication).
24. D. J. Weidner and Y. Wang, *J. Geophys. Res.* **103**, 7431 (1998).
25. Weidner and Wang (24) computed density and velocity profiles through the 660-km discontinuity for several different models of mantle composition (with differing Al content) and temperature (1700, 1900, and 2100 K). The points labeled "Pyr" in Fig. 3B are for their 5% Al model at 1700 K; for this model, the velocity and density jumps occur across an interval of less than 20 km. Some of the other models have more gradual gradients that cannot be directly converted to points on Fig. 3. We tested to see if these models might fit our data by computing synthetic seismograms based on the profiles in Fig. 4 of Weidner and Wang (24). All of these models grossly overpredict our observed *S660S* and *P660P* amplitudes and lie outside the error bars plotted in Fig. 2.
26. P. M. Shearer, *Nature* **344**, 121 (1990).
27. S. M. Ridgen *et al.*, *ibid.* **354**, 143 (1991).
28. This work was supported by NSF grants EAR93-15060, EAR95-07994, EAR96-14350, and EAR96-28020. M.P.F. was supported by an NSF Postdoctoral Fellowship and the Cecil H. and Ida M. Green Foundation. J. Gaherty and J. Vidale provided constructive reviews of an earlier version of this report.

28 April 1999; accepted 13 July 1999

# Improved Weather and Seasonal Climate Forecasts from Multimodel Superensemble

T. N. Krishnamurti,<sup>1</sup> C. M. Kishtawal,<sup>1</sup> Timothy E. LaRow,<sup>1</sup> David R. Bachiochi,<sup>1</sup> Zhan Zhang,<sup>1</sup> C. Eric Williford,<sup>1</sup> Sulochana Gadgil,<sup>2</sup> Sajani Surendran<sup>2</sup>

A method for improving weather and climate forecast skill has been developed. It is called a superensemble, and it arose from a study of the statistical properties of a low-order spectral model. Multiple regression was used to determine coefficients from multimodel forecasts and observations. The coefficients were then used in the superensemble technique. The superensemble was shown to outperform all model forecasts for multiseasonal, medium-range weather and hurricane forecasts. In addition, the superensemble was shown to have higher skill than forecasts based solely on ensemble averaging.

Sophisticated numerical models used in operational and research centers throughout the globe routinely make short-term (1 to 7 days in advance) weather and seasonal (one to several seasons in advance) climate forecasts. Individually each modeling group tracks the forecast skill of their model. Within recent years, the use of model ensembles has become an important forecasting component. The methodology of how to generate the ensemble is the focus of many forecasting centers. Here we show that a multimodel

superensemble can more accurately predict weather and seasonal climate. The superensemble is developed by using a number of forecasts from a variety of weather and climate models. Along with the benchmark observed (analysis) fields, these forecasts are used to derive simple statistics on the past behavior of the models. These statistics, combined with multimodel forecasts, enable us to construct a superensemble forecast.

Given a set of past multimodel forecasts, we used a multiple regression technique (for the multimodels), in which the model forecasts were regressed against an observed (analysis) field. We then used least-squares minimization of the difference between the model and the analysis field to determine the

<sup>1</sup>Department of Meteorology, Florida State University, Tallahassee, FL 32306, USA. <sup>2</sup>Center for Atmospheric and Oceanic Sciences, Indian Institute of Science, Bangalore, India.